Vol. 47, No. 1 (2025) 77-91, DOI: 10.24874/ti.1836.12.25.01

Tribology in Industry

www.tribology.rs

RESEARCH

Coupled SPH-FEM Simulation Model to Analyze the Mechanism of Single Particle Impact in Abrasive Waterjet Machining

Y. Abdelhameed[a,b,*], Ibrahem Maher[a,c], Jiwang Yan[d], Hassan El-Hofy[e], Mohsen A. Hassan[a]

[a]*Industrial and Manufacturing Engineering Dept., Egypt-Japan University of Science and Technology (E-JUST), 21934, Borg El Arab, Egypt,*
[b]*Department of Mechanical Engineering, Benha Faculty of Engineering, Benha University, 13512, Benha, Egypt,*
[c]*Department of Mechanical Engineering, Faculty of Engineering, Kafrelsheikh University, 33516, Kafrelsheikh, Egypt,*
[d]*Department of Mechanical Engineering, Faculty of Science and Technology, Keio University, 223-8522, Yokohama, Japan,*
[e]*Department of Production Engineering, Faculty of Engineering, Alexandria University, 21544, Alexandria, Egypt.*

Keywords:

Abrasive waterjet
Coupled SPH-FEM model
Numerical simulation
Particle impact
Erosion mechanism

* Corresponding author:

Y. Abdelhameed
E-mail:
yahya.abdelhameed@bhit.bu.edu.eg

Received: 23 December 2024
Revised: 6 January 2025
Accepted: 31 January 2025

A B S T R A C T

Studying single particle impact is crucial to understanding the erosion mechanism in abrasive waterjet machining (AWJM). In this paper, the finite element method (FEM) and smoothed particle hydrodynamics (SPH) were combined to investigate the mechanism of single particle impact under the waterjet influence. The particle (garnet) and workpiece (Al 7075-T6) were represented by FEM, while the waterjet was discretized using SPH. Linear elasticity and the Johnson-Cook (JC) model were selected to model the abrasive and workpiece materials, respectively. The simulation was conducted in ABAQUS where the effects of particle shape, position, and impact angle on material removal were investigated. The results of the developed model revealed that the erosion mechanism and mechanics significantly differed when considering the waterjet effect. This was primarily attributed to the dynamic phenomena resulting from the waterjet impact, including stagnation zone and drag forces. It was found that the impact angle corresponding to maximum erosion depended on the particle shape and radial position within the jet stream. The presented model has proved its capability since it offers a novel perspective on the single particle impact mechanism by incorporating the realistic dynamic phenomena accompanying the impact in AWJM.

1. INTRODUCTION

The increasing technological demands in industry have paved the way for abrasive waterjet machining (AWJM) to play a prominent role among machining technologies. This technology utilizes a fluid-particle interaction to accelerate the abrasive particles towards the workpiece. The kinetic energy of high-speed accelerated particles is fair enough to erode

almost all engineering materials regardless of their mechanical properties. Several wear mechanisms, such as deformation and cutting wear, govern the erosion process in ductile materials [1]. The erosion performance in AWJM is dependent on many parameters such as waterjet pressure, abrasive mass flow rate, workpiece motion, nozzle specifications, impact angle, and standoff distance (SOD). Further, abrasive characteristics, such as shape, mesh size, hardness, and sharpness, also affect erosion [2]. Several abrasive materials are used in AWJM such as garnet, boron carbide, and alumina oxide, among which garnet is the most common. AWJM proved its superiority with many advantages, including no thermal or mechanical distortion, low cutting forces, ability to machine intricate shapes, and diversity of machining operations [3]. Hence, it is extensively employed in several industries, such as aerospace, automotive, construction, oil, and medical.

The impact of abrasive particle is the main event responsible for erosion in AWJM. While this erosion is advantageous for material removal in machining applications, it can also be detrimental, as it leads to wear on critical components such as the focusing tube within the machine system [4,5]. Comprehending the impact mechanism of a single particle would be crucial for optimizing AWJM efficiency. By elucidating how particle kinetic energy is converted into workpiece deformation and material removal under various conditions, this knowledge can guide the selection of optimal process parameters, improve energy utilization, and minimize nozzle wear. Hence, an urgent need is to find efficient methods capable of thoroughly revealing the sophisticated erosion mechanisms due to particle impact. A broad range of analytical models were proposed to analyze the workpiece surface erosion, considering various factors [2]. However, the extreme complexity of such models, necessitating many simplification assumptions, limits their flexibility and reliability.

Numerical modeling always remains attractive for investigating and predicting the performance of nonlinear complex processes. A wide range of numerical tools were applied to examine and analyze the erosion mechanisms of AWJM due to single particle impact. Hassan and Kosmol [6] earlier developed a model using the finite element method (FEM) to simulate the mechanism of the single particle impact on a carbon steel workpiece. Junkar et al. [7] utilized the same method to investigate the crater sphericity under different impact speeds and angles. Yıldırım and Müftü [8] reported that the erosion results due to particle impact were relying on the smoothness of the struck surface. Dong et al. [9] coded a Fortran program to reveal the basic mechanisms of erosion at low impact speeds employing the SPH method. Abdelhameed et al. [10] proposed a numerical model based on the FEM to investigate the effect of using different material models for garnet abrasive.

Up to now, all numerical models developed to simulate the erosion mechanism of single particle impact have neglected the effect of the waterjet. Despite that, some models addressing multi-particle impacts have incorporated the waterjet effect. Dong et al. [11] included the waterjet-particle interaction in simulating the impact of triangular abrasive particles. Nyaboro et al. [12] constructed a computational fluid dynamics (CFD) model that demonstrated the jet dynamic flow, tracked the abrasive particles, and predicted the ER. Du et al. [4] integrated three techniques: FEM, SPH, and discrete element method to conduct a whole-stage simulation for AWJM. Du et al. [13] established a 2D coupled model using FEM and SPH to explore the kerf geometry resulting from the impact of irregular polyhedron particles on Ti6Al4V and AISI 304. Another SPH-FEM-based model, developed by Vasudevan et al. [14], was devised to analyze hole diameter and shear stress while piercing small holes in nickel superalloys.

In conclusion, the erosion mechanism of AWJM underlies multi-dynamic impacts that result in high strain rates and large deformations. Despite numerous attempts to analyze the single particle impact in AWJM, the dynamic effect of the waterjet on this mechanism has been overlooked. In this paper, FEM and SPH methods were coupled to comprehensively mimic the mechanics of a single particle impact under the waterjet effect. This coupled analysis can retain the advantages of both techniques, i.e., the high efficiency of FEM in solid mechanics and the reliability of SPH in simulating the flow/impact of the waterjet. By providing a precise and deeper understanding of the realistic impact mechanism in AWJM, the proposed model can facilitate the selection of optimal machining factors, thereby enhancing the efficiency of the AWJM process.

2. COUPLED SPH-FEM MODEL

A new coupled SPH-FEM model was developed and presented to simulate the impact of a particle within the injection-type of AWJM. The well-established FEM was involved in discretizing the eroded workpiece and abrasive particle using the conventional Lagrangian formulation. Unlike the previous models of single particle impact, the SPH technique was utilized to capture the realistic waterjet effect on the particle impact. This would improve the modeling accuracy of the erosion mechanism, as the waterjet plays a crucial role in accelerating the abrasive particle and affecting its trajectory before the impact event. The workpiece material was assigned as Al 7075-T6 alloy, and the selected type of abrasive was garnet of #80 size. The variable simulation parameters are listed in Table 1. Four particle shapes were considered for the abrasive particle. Material modeling, model geometry, assembly, discretization, interactions, initial and boundary conditions were thoroughly discussed in the following sub-sections.

Table 1. Parameters used in numerical simulation.

Model parameters	Unit	Levels
Particle vertical distance	mm	0.1, 0.2, 0.3, 0.4, 0.5, 1, 1.5, 2, 2.5, 3
Particle radial position (R_p)	mm	0, 0.21, 0.42, -0.42
Impact angle (θ)	deg	30, 45, 60, 75, 90
Traverse speed (v_f)	mm/s	0, 1, 5, 25, 125
Waterjet pressure (P)	MPa	300
Abrasive mesh (#)	-	80
Jet diameter	mm	1.02
Orifice diameter	mm	0.35

2.1 Principles of SPH formulation

SPH is a numerical approach defined as a meshless particle method based on the Lagrangian formulation [15]. This technique discretizes the continuum domain into a set of arbitrarily distributed particles. Therefore, there is no need for the connectivity matrix that is essentially required for storing the element neighborhoods' information during every step in the FE-simulation process. In SPH analysis, each particle carries the continuum properties and possesses its physical quantities such as mass, velocity, acceleration, and energy [16]. SPH formulation starts with using a kernel approximation scheme to interpolate the required field variables at any point in the computational domain. Hence, the approximation of a continuous variable field function *f(x)* can be expressed using the formula [15] shown in the equation (1).

$$f(x) = \int_{\Omega} f(x')\, W(x - x', h)\, dx' \qquad (1)$$

where x denotes the particle position in the computational domain Ω, W is the kernel function, and h is the smoothing length. The kernel function should satisfy the condition of the Dirac delta function at a smoothing length of zero. The continuous function form can be rewritten into a discrete particle approximation, as follows:

$$f(x) \simeq \sum_{j=1}^{n} m_j \frac{f(x_j)}{\rho_j} W\left(x - x_j, h\right) \qquad (2)$$

where $f(x_j)$ is the approximate function value at a neighboring particle j, m_j is the mass of that particle, ρ_j is its density, n is the number of neighboring particles. In this paper, the quadratic kernel function was adopted because of its stability in high-speed impact problems and its capability of handling the issue of compressive instability [15]. The kernel equation is presented in equation (3).

$$W(R, h) = \alpha_d \left(\frac{3}{16}R^2 - \frac{3}{4}R + \frac{3}{4}\right) \qquad (3)$$

where $\alpha_d = 1/h,\ 2/\pi h^2$, and $5/4\pi h^3$ in 1D, 2D, and 3D spaces, respectively, and R denotes the relative distance between two particles ($0 \le R \le 2$). A variable smoothing length was employed to stabilize the number of contributing particles.

2.2 Material modeling

Al 7075-T6 is a high-strength aluminum alloy of moderate ductility, widely used in aerospace and automotive applications. The Johnson-Cook (JC) strength model [17] was adopted for this alloy because it reliably describes the behavior of such materials undergoing high strain rates [6]. Since AWJM does not generate significant temperature, the model was simplified by deleting the thermal softening term. Hence, the modified model is given in equation (4).

$$\sigma = [A + B\varepsilon^n]\left[1 + C\, ln\left(\frac{\dot{\varepsilon}}{\dot{\varepsilon}_0}\right)\right] \qquad (4)$$

where σ is the flow stress and ε is the equivalent plastic strain, $\dot{\varepsilon}$ is the plastic strain rate, $\dot{\varepsilon}_0$ is the initial strain rate, A, B, C, and n are the relevant material constants.

The JC failure criterion [18] was used and also amended by neglecting the thermal softening; hence, the failure strain can be given as follows:

$$\varepsilon_f = \left[D_1 + D_2 e^{D_3 \sigma^*}\right]\left[1 + D_4 \, ln\left(\frac{\dot{\varepsilon}}{\dot{\varepsilon}_0}\right)\right] \quad (5)$$

where σ^* is the ratio of hydrostatic stress to von Mises equivalent stress and D_1-D_4 are damage constants. The damage initiation can be decided according to the cumulative damage D that equals the term $\sum \Delta\varepsilon/\varepsilon_f$. The JC constants of Al 7075-T6 are listed in Table 2. The Mie–Gruneisen equation of state (EOS) defining the pressure-volume relationship was integrated with JC material model, and its constants were C_0 = 5240 m/s, S = 1.4, and Γ_0 = 1.97 [19].

Table 2. The constants of JC material and fracture models of Al 7075-T6 [20].

Material property	Unit	Al 7075-T6
Density (ρ)	kg/m³	2700
Shear modulus (G)	GPa	26.3
Yield strength (A)	MPa	473
Hardening constant (B)	MPa	210
Hardening exponent (n)	-	0.3813
Strain rate constant (C)	-	0.033
Damage parameter (D_1)	-	0.3714
Damage parameter (D_2)	-	-0.1233
Damage parameter (D_3)	-	-1.9354
Damage parameter (D_4)	-	0.0101

Garnet is the most common abrasive type utilized in AWJM. This can be attributed to its favorable properties, such as high hardness (around 7-7.5 on the Mohs scale), high density, and economic viability. Hence, this material was chosen for the abrasive particle. Following most prior numerical research, which employed rigid or linear elastic models for garnet material, a linear elastic model was employed for modeling the abrasive particle. Table 3 illustrates the assigned material constants for the garnet abrasive.

Table 3. Material parameters of garnet [21].

Material property	Unit	Garnet
Density (ρ)	kg/m³	4120
Elastic modulus (E)	GPa	248
Poisson's ratio (v)	-	0.3

The linear EOS of Mie–Gruneisen is suitable for describing the behavior of incompressible inviscid fluid flow governed by the Navier-Stokes equation of motion [22]. Accordingly, the dynamic viscosity was integrated with the Mie–Gruneisen EOS to define the waterjet. The material coefficients used for modeling waterjet are listed in Table 4.

Table 4. Material coefficients of waterjet [23].

Material property	Unit	Water
Density (ρ)	kg/m³	1000
Sound speed (C_0)	m/s	1450
EOS material constant (S)	-	0
EOS material constant (Γ_0)	-	0
Dynamic viscosity (η)	Pa.s	1.14×10^{-3}

2.3 Model generation

The explicit dynamic module provided by the commercial software ABAQUS was introduced in the current investigation to implement and simulate the numerical model. Since the research aims to imitate the fluid-solid interaction in AWJM, the created 3D model mandatorily included three instances: target part, abrasive particle, and waterjet, as shown in Fig. 1. The target was modelled as a rectangular shape with dimensions of 4.5 × 1.25 × 3.5 mm³. A cylindrical shape having a diameter of 1.02 mm (jet diameter) and length of 4 mm was set for the waterjet.

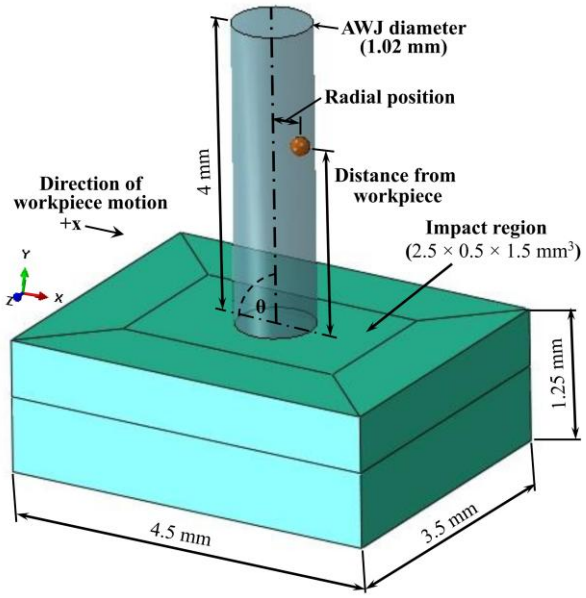

Fig. 1. Model geometry and assembly.

Table 5. Shapes of abrasive particles.

Used shapes	Sphere	Trapezoidal prism	Triangular prism	Icosahedron
			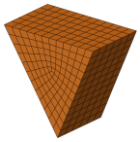	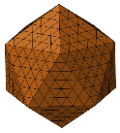
Features	Diameter	Base length, height	Base length, depth	Edge length
Size (μm)	180	164.3	241.6, 120.8	111.9

The erosion mechanism is significantly affected by the shape of the impacting abrasive particle [24]. Hence, four shapes were considered, as shown in Table 5, to represent different modes of erosion when the target engages with curved surfaces, flat surfaces, sharp edges, and acute vertices. It was reported that the size and shape distribution of abrasive particles randomly varies due to the mixing process inside the focusing tube [25,26]. However, a constant particle diameter of 180 μm, corresponding to the average particle size of mesh #80, was utilized for model simplification.

A convergence analysis was performed to assign the element size in the refined mesh region where the impact occurs. This analysis was conducted using six sizes of mesh, starting with a coarse size of 60 μm and ending with a fine mesh size of 10 μm. The variations of maximum strain energy and computational time were evaluated, as illustrated in Fig. 2. The maximum strain energy exhibited a good convergence at the fifth mesh size (20 μm) while maintaining a proper computational time, hence, this mesh size was chosen in this study.

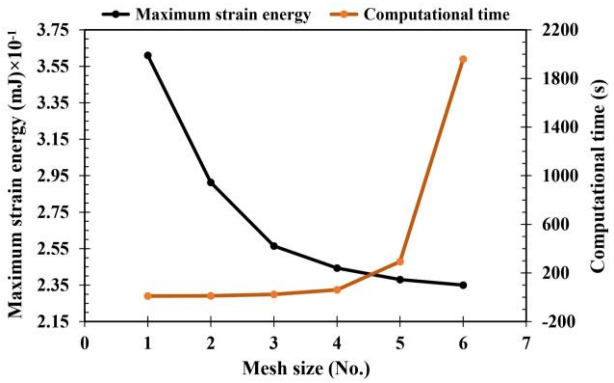

Fig. 2. Mesh sensitivity analysis (maximum strain energy within the whole model).

The mesh size of abrasive particles was also set as 20 μm. Both workpiece and abrasive particles were meshed using linear 3D stress elements (C3D8R) with default hourglass control. The element deletion option was applied to retain the stability and cost of the simulation by allowing the removal of highly distorted elements. On the other hand, the waterjet was discretized using SPH particles of type PC3D. The distance between the neighbored smoothed particles was set to 18 μm. The workpiece was meshed by 329,875 elements of them 234,375 for the impact zone. The number of SPH particles was 172,470 per 1 mm of jet length. A closeup of the model discretization strategy is depicted in Fig. 3.

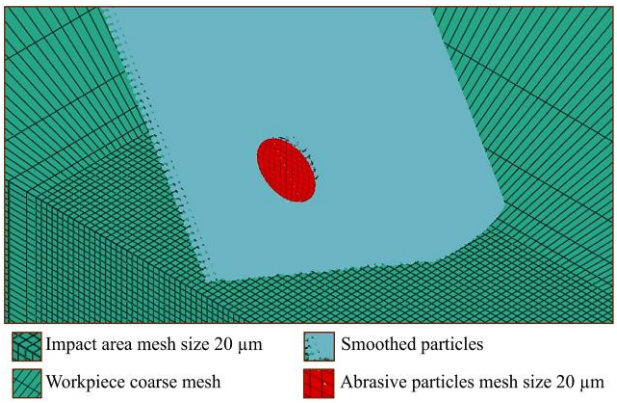

Fig. 3. A cross-sectional view showing the discretizing strategy of the model.

The general contact algorithm was selected to include all interacting surfaces. The tangential interaction behavior between the workpiece and abrasive particles was defined using a penalty-based coefficient of friction equal to 0.1. Meanwhile, the interaction between the waterjet and other model surfaces was realized by utilizing both tangential frictionless and normal hard-contact behaviors in parallel.

The bottom workpiece surface was constrained in y and z directions while it was allowed to move in the x direction at a speed equal to the traverse rate.

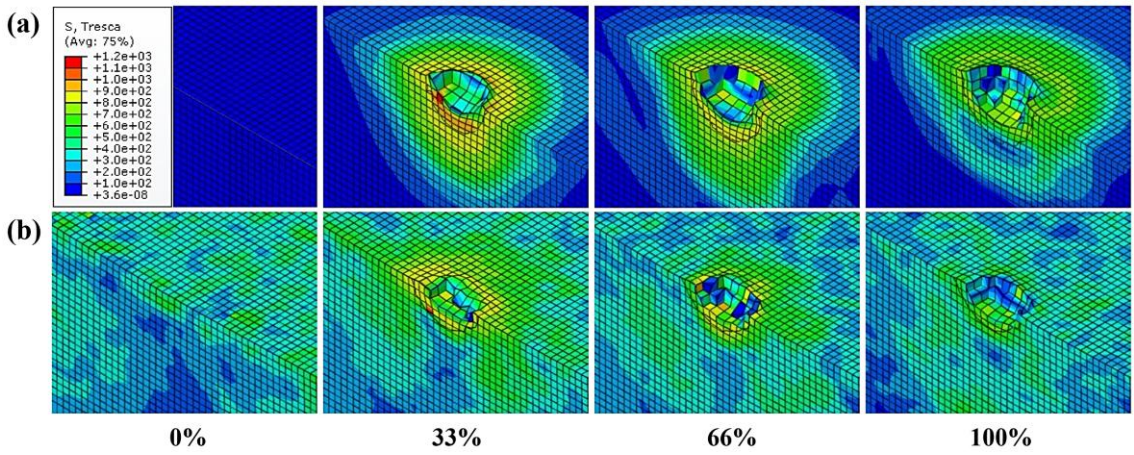

Fig. 4. Evolution of crater throughout the erosion time, (a) solo particle impact, (b) waterjet inclusion.

The initial waterjet velocity (v_w) was obtained based on Bernoulli's equation as follows:

$$v_w = \varphi \sqrt{\frac{2P}{\rho_w}} \quad (6)$$

where P is the waterjet pressure, ρ_w is the water density, and φ is the coefficient of momentum loss which typically ranges from 0.88 to 0.95 [1]. The momentum transfer from the waterjet to the abrasive particles [21] was considered while calculating the initial speed of abrasive particles, as in equation (7).

$$v_a = \left[\left(\frac{\dot{m}_a}{\dot{m}_w}\right)^2 - 1.57\left(\frac{\dot{m}_a}{\dot{m}_w}\right) + 0.8861\right] v_w \quad (7)$$

where $\dot{m}_w$ is the mass flow rate of water and $(\dot{m}_a/\dot{m}_w)$ is the abrasive load ration. The particle was allowed to travel using the calculated speed (v_a) where its vector was decomposed into x and y components according to the used impact angle.

3. RESULTS AND DISCUSSION

In the present study, eight test groups (108 tests) were constituted where the initial velocities of waterjet and abrasive particles were 720.4 m/s and 638.4 m/s, respectively. Different particle parameters, such as shape, impact angle, and position, were considered along with the traverse rate of the workpiece. All simulations were solved using the explicit dynamic solver of ABAQUS while activating the double precision option. They were run on a desktop computer equipped with Intel® Xeon® Processor E5-2690 v3 (12 cores) and 32 GB RAM. The step time of simulations was calculated as the distance between the workpiece surface and abrasive particle divided by the velocity of this particle.

3.1 The effect of waterjet inclusion

In simulation, the impact velocity of abrasive particles and the resulting erosion were analyzed with and without waterjet. Ten vertical distances between the abrasive particle and workpiece surface were considered while initially positioning the particle inside the waterjet. Particle vertical distances were 0.1, 0.2, 0.3, 0.4, 0.5, 1, 1.5, 2, 2.5, and 3 mm. Three radial positions of 0, 0.21, and 0.42 mm were assigned to the abrasive particles. Jet diameter, traverse speed, and impact angle were kept at 1.02 mm, 0 mm/s, and 90°, respectively. Whereas a spherical particle was used to study the effect of waterjet inclusion.

The evolution of eroding action of single particle is presented in Fig. 4 at 0%, 33%, 66%, and 100% of the total erosion time. Particle vertical distance and radial position were 0.5 mm and 0 mm, respectively. Fig. 4 (a) shows the crater evolution with no waterjet inclusion, while Fig. 4 (b) considers the addition of waterjet to the simulation model. With the advancement of simulation time, the depth and volume of the crater were increased until the particle kinetic energy contributing to material removal diminished. The color bar shows a significant difference in the induced shear stresses at different impact events. Higher stress values and wider stressed regions have been observed in the particle impact without waterjet compared to the particle impact with waterjet inclusion. Consequently, a higher material removal rate with a percentage of 39.1% was obtained, achieving a larger and deeper crater, as depicted in Fig. 4(a). This may be attributed to the loss in particle kinetic energy due to the waterjet damping after its impact with the workpiece, meaning limited amount of transferred kinetic energy from the particle to the workpiece.

To thoroughly identify the effect of waterjet inclusion on the dynamics of the abrasive particle, the instantaneous impact velocity of particle was tested under different vertical and radial positions, as shown in Fig. 5. It is apparent that the impact velocity varies according to the particle position within the waterjet. At a radial position of zero, the impact velocity was decreased as the particle is positioned farther away from the workpiece surface. However, starting from a 0.5 mm vertical distance, the impact velocity insignificantly fluctuates at an average velocity of 470 m/s, much lower than the theoretical impact velocity (638.4 m/s) when no waterjet is considered. The same trend occurs at radial positions of 0.21 and 0.42 mm but higher average velocities of 490 m/s and 530 m/s, respectively, were predicted. It can be concluded that a higher erosive capability is acquired when the particle is located close to the jet periphery, yet lower ERs are still realized compared to theoretical rates. Hence, employing theoretical impact velocities in simulating AWJM may attain misleading results of ERs that radically differ from the realistic conditions.

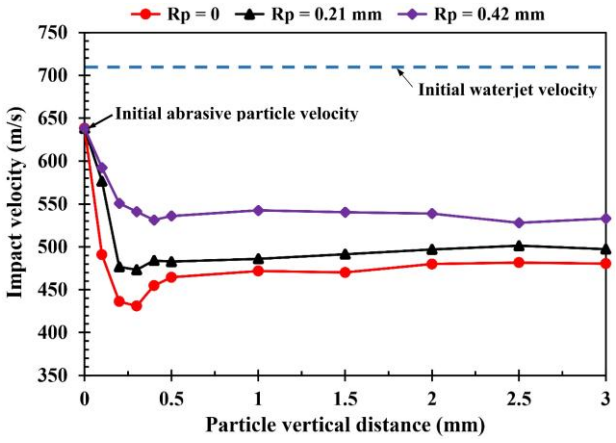

Fig. 5. Variation of particle impact velocity with the vertical position at three different radial positions.

Fig. 6 depicts the profile of particle kinetic energy throughout the simulation time, to explore the reason for the variance between theoretical and actual impact velocities, at 1.5 mm vertical distance and 0 mm radial position. In this figure, the associated color map shows the velocity magnitude (mm/s) of the waterjet and abrasive particle. Fig. 6 (a) shows the initial position of the abrasive particle within the waterjet. Figs. 6 (b-e) present the formation of the stagnation zone near and above the workpiece surface due to the impact of the waterjet. This zone was found because of the hydraulic shock generated by the waterjet strike on the target surface. Initially, the waterjet continually accelerated the particle for 1.15 μs till reaching the region shown in Fig. 6 (b), where the abrasive particle velocity was recorded as 661 m/s. In this region, a slight reduction in the waterjet velocity was observed as nearing the workpiece surface where the stagnation zone exists. Thus, the particle was gradually slowed down recording a velocity of 617 m/s, at the position indicated in Fig. 6 (c). There, the particle entered the stagnation zone getting closer to the workpiece surface; consequently, the deceleration rate of the abrasive particle became steeper. As a result, the particle velocity was significantly reduced to 470.1 m/s, just before the impact event, as found in Fig. 6 (d). The remaining kinetic energy of the impacting abrasive particle is almost completely lost in the collision with the workpiece, as demonstrated in Fig. 6 (e).

As evident, the stagnation zone is typically a region of low flow velocity, created within the jet stream upon its impact. This low-velocity region disrupts the forward kinetic energy of the abrasive particles traveling within the jet. Moreover, the complex flow within this zone can exert some forces on the particles, altering their trajectories and reducing their impact velocity. Hence, the particle erosive efficiency was reduced since the erosion process in AWJM primarily relies on the kinetic energy of the impacting particles. This reduction was dependent on the particle radial position due to variations in the intensity of the stagnation zone across the jet cross-section. Some previous studies [11, 27, 28] also reported this phenomenon. Despite that, its effect on particle movement and erosion was either neglected or marginalized. The influence of this phenomenon was not previously examined using experimental investigations because it is extremely difficult to measure the instantaneous particle velocity just before the impact occurs. This is attributed to the highly dynamic, erosive, and deflective nature of the abrasive waterjet upon impact, which can cause serious damage for measurement devices. Thus, our numerical model is very useful since the experimental investigation of particle impact mechanics is very difficult and expensive.

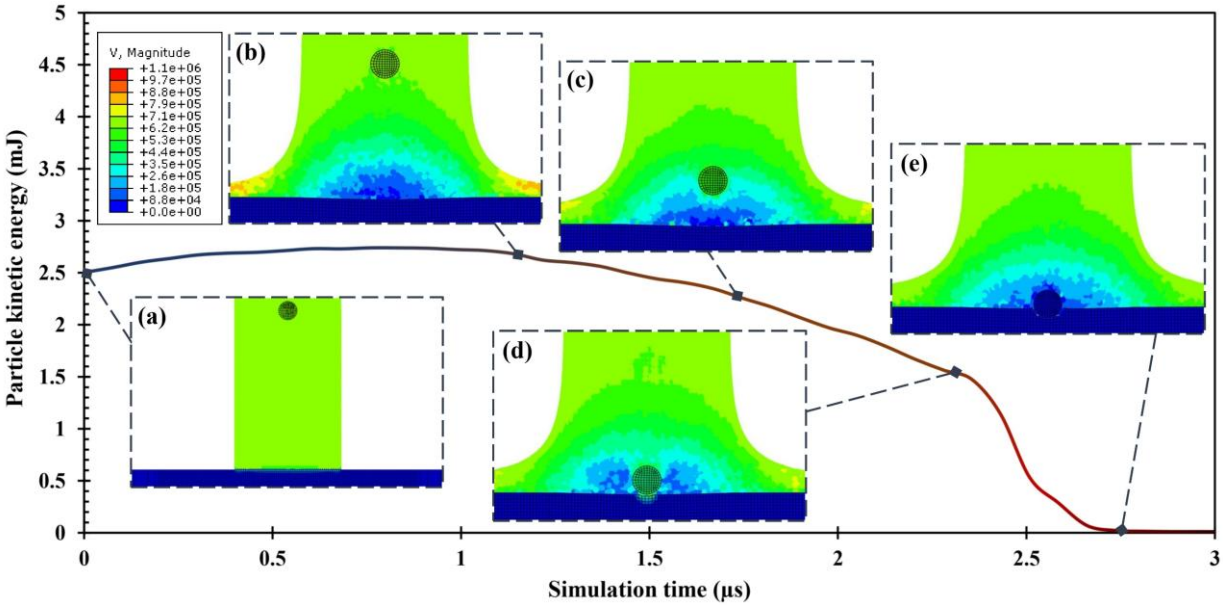

Fig. 6. The profile of particle kinetic energy throughout the simulation time at 1.5 mm particle vertical distance and zero radial position.

In order to predict and examine the material removal, the eroded volume due to single particle impact was quantified through multiplying the element volume by the number of fractured elements. Fig. 7 highlights the effect of vertical particle position on the removed volume of material at 0 mm radial position. It is conspicuous that the eroded volume and particle impact velocity had the same trend, meaning that the material removal systematically responds to the change in particle kinetic energy. Moreover, the eroded volume varied under different vertical positions until reaching an average of 740,000 μm^3 starting from 0.5 mm. It can be deduced that each particle impact would attain different material removal according to its position within the waterjet stream.

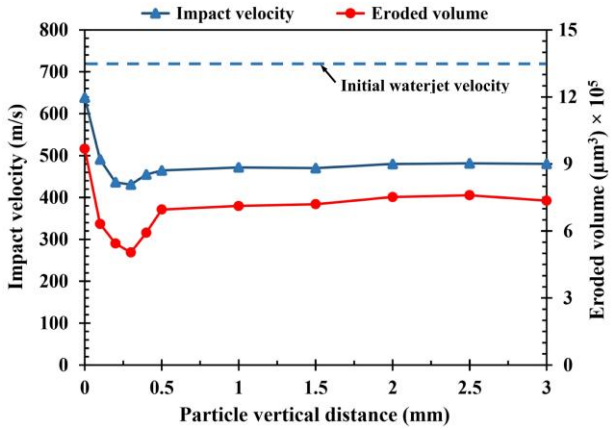

Fig. 7. The effect of vertical position on the eroded volume and particle impact velocity at R_p = 0.

Additionally, the ER at the waterjet periphery is predicted to be larger than the jet center, which complies with the numerical findings reported in ref [29]. Nevertheless, the experimental AWJM involves multiple impacts of abrasive particles that are normally distributed around the jet center. Besides, the initial velocities of the abrasive particles escaping the nozzle are higher the closer to the middle of jet. Therefore, as in practice, the relatively high ERs at the jet center in AWJM can be achieved by combining the individual particle mechanism and the realistic distribution of the abrasive particles.

3.2 The effect of traverse speed

Traverse rate is one of the key factors that influences the kerf generation in AWJM. In this section, the eroded volume of material was investigated 0, 1, 5, 25, 125 mm/s workpiece traverse speeds. It is worthwhile noting that similar values are frequently used in different AWJM applications. However, the investigated range (0-125 mm/s) is practically not used for a single AWJM application. This range was specially chosen in this study to clarify whether the traverse speed significantly affects the erosion mechanism on single particle impact. The initial vertical position of the impinging particle was maintained at 0.5 mm. Fig. 8 assures that the effect of traverse speed on the erosion process is insignificant even on a wide range. This may be attributed to the large difference in the ratio of the instantaneous particle impact velocity and the motion speed of

the workpiece. For instance, the ratio between the minimum impact velocity and maximum traverse rate was 3,450 while it reached 540,000 when dividing the maximum impact velocity by the minimum traverse rate. Therefore, it is expected that the traverse speed can only control the overlapping extent of multiple particle impact but with no remarkable effect on the material removal mechanism.

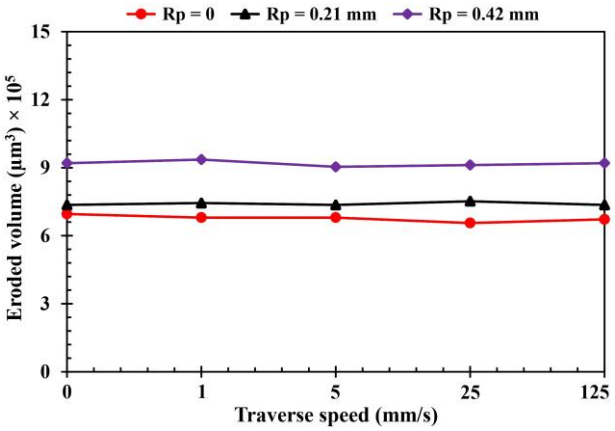

Fig. 8. The effect of the workpiece traverse speed on the eroded volume at 0.5 mm particle vertical distance and three radial positions.

3.3 The effect of impact angle

Once the jet is tilted, the impact dynamics become asymmetric about the central jet axis, as depicted in Fig. 9. This induces uneven pressure and velocity distributions within the jet stream, causing the stagnation zone to shrink and shift towards the inclination direction. Since this asymmetry affects the zone size and position, its damping effect becomes more dependent on the impact position of the abrasive particle. Fig. 9 indicates that the size of the stagnation zone contracted as the impact angle reduced from 90° to 30°. Meanwhile, with angle reduction, the zone position gradually shifted far away from the jet center. To investigate the effect of jet tilting on the impact mechanism, the eroded volume and particle rebound energy were studied at 30°, 45°, 60°, 75°, and 90° impact angles. New three radial positions (0, 0.42, and -0.42 mm) were considered to examine the non-symmetry of jet dynamics.

Fig. 10 shows the effect of jet impact angle on the eroded volume resulting from the single impact of a spherical particle. It is revealed that the maximum eroded volume at 0 mm and 0.42 mm radial positions was obtained at an impact angle of 60°, whilst it was found at 45° for R_p = -0.42 mm and excluded-waterjet impact. At a radial position of zero, a higher removal was achieved at angles 45° and 60° compared to the case of waterjet exclusion. Except for R_p = -0.42mm, it can be declared that the effect of impact angle on the eroded rate has the same trend at all radial positions: the eroded volume gradually increased till its maximum at an impact angle of 60° and then steadily decreased. However, at R_p = -0.42 mm, the erosion is maximized at 30° and 45° due to the minimal influence of drag forces and stagnation zone. Overall, tilting the jet improves the particle potency of erosion across most impact angles compared to the condition of no waterjet. This aligns with the observation that the stagnation zone effect almost diminished at shallow angles, allowing better kinetic energy transfer. In contrast, this does not apply for the 30° impact angle, specifically at 0 mm and 0.42 mm radial positions, as the increased drag forces limited energy transfer to the workpiece.

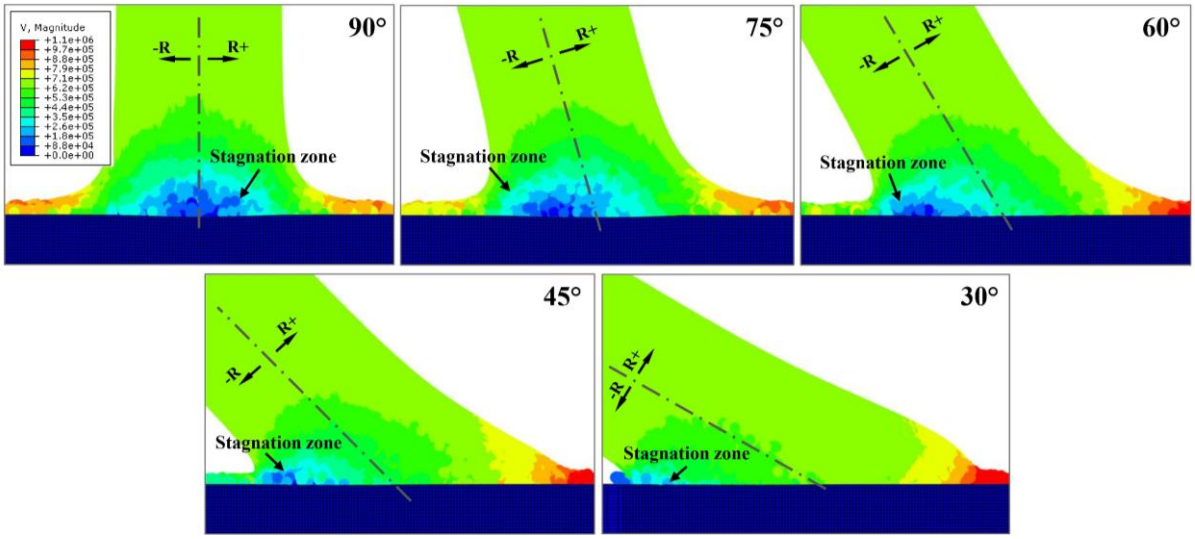

Fig. 9. The effect of the jet impact angle on the formation of the stagnation zone.

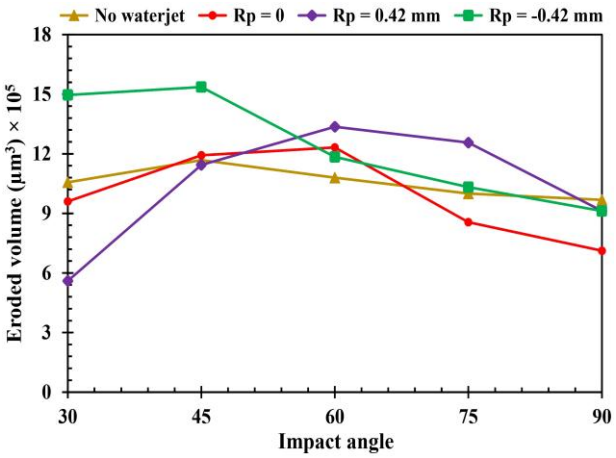

Fig. 10. Variation of eroded volume with impact angle at 0.5 mm vertical distance and three radial positions.

It is well known that not all particle energy contributes to the material removal of the workpiece material. Hence, the effect of impact angle on the extent of particle rebound energy was investigated to explore its influence on the erosion efficiency. Fig. 11 manifests the combined influence of jet impingement angle and radial position on particle rebound energy. It can be observed that the shallower the impact angle, the higher the particle rebound energy. A better kinetic energy transfer was realized as the impact angle came closer to 90°, i.e., the jet is perpendicular to the workpiece surface. Despite the previous observation, the material removal did not reach its maximum value at an angle equal to 90° because most of particle kinetic energy contributed to compress the workpiece material rather than shearing it. Thus, the maximum removal rate was found at the impact angles of 45° and 60°, where a proper amount of kinetic energy was mainly applied through shearing action for material removal.

Generally speaking, tilting the waterjet creates an asymmetric velocity distribution around the jet's central axis, disrupting the uniformity of the flow dynamics. Furthermore, it generates more lateral flow, which increases shear forces acting on the waterjet flow, and thus introduces more drag forces. Under specific conditions, the interplay between the induced stagnation zone and drag forces can create an optimal impact angle and maximum impact velocity, optimizing particle erosion. Conversely, minimum erosion can be obtained in two cases. The first occurs at the jet center under conditions of no jet tilting and minimal drag forces, where the stagnation effect is most pronounced. The second occurs at the jet periphery when the jet is highly inclined, leading to maximum drag forces and significantly altering the particle impact trajectory, resulting in the least favorable impact angle. These findings can be leveraged to optimize process conditions for achieving maximum material removal rates.

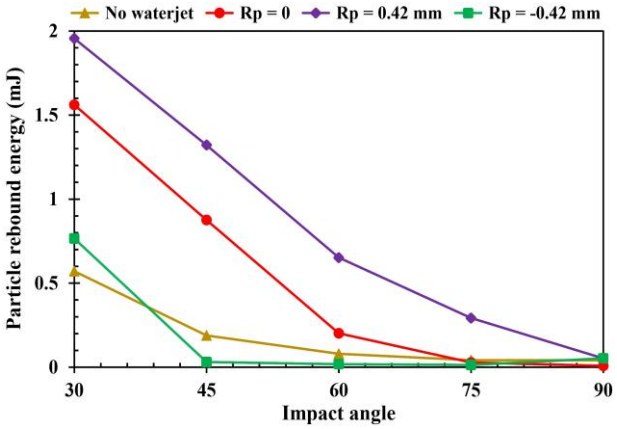

Fig. 11. The influence of impact angle on particle rebound energy at 0.5 mm particle vertical distance and three radial positions.

3.4 The effect of particle shape

The crater morphology and eroded volume were investigated by exploiting four shapes of abrasive particles: spherical, trapezoidal, triangular, and icosahedron. Five impact angles and three radial positions were considered while other parameters were kept unchanged. The change in crater morphology is presented in Fig. 12 at a zero-radial position. It can be recognized that deeper craters were given at 60° and 75°, while wider craters emerged at 30° and 45°. Using trapezoidal and triangular particles, deeper craters were obtained since these shapes involved a single sharp edge in the erosion process acting like a cutter tool. Generally, sharp-edged particles, such as the trapezoidal, triangular, and icosahedron particles, guarantee a higher average of material removal. This can be attributed to the fact that sharp-edged particles concentrate the impact force on a tiny contact area, leading to higher localized stresses. Moreover, the sharp edges introduce a cutting rake angle which stimulates the cutting mechanism and so the erosion.

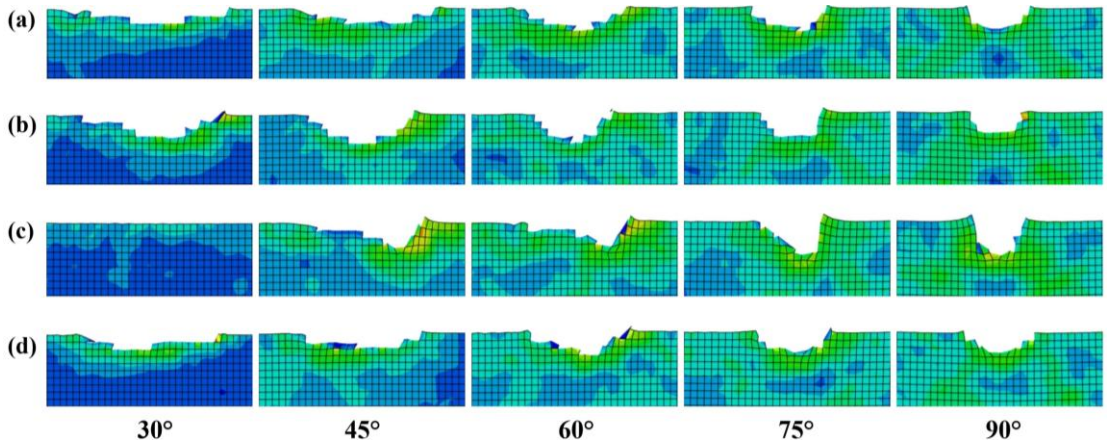

Fig. 12. Comparison of crater morphology at different impact angles and particle shapes, (a) spherical, (b) trapezoidal, (c) triangular, (d) icosahedral.

The eroded volume was examined for different impact angles and radial positions, as illustrated in Fig. 13. The numerical predictions show that the interacting effect of impact angles and radial positions created random variations regarding the ERs, especially for trapezoidal and triangular particles. This is attributed to the change in particles orientations resulted from varying the impact angles and radial positions simultaneously. Since the spherical and icosahedral particles have uniform and axisymmetric shapes, their erosion curve showed minimal random fluctuations, unlike the observed for the other particle shapes. It can be concluded that the maximum eroded volume occurred at 30° for trapezoidal and 45° for spherical, triangular, and icosahedral particles. This was achieved at -0.42 mm radial position because of the minimized influence of both stagnation zone and drag forces. The lowest ERs for all particle shapes, except for triangular, were achieved at 90°. On the other hand, regarding the triangular particle, zero erosion occurred at a 30° angle due to the significant influence of drag forces on its shape. In general, better erosion performance is realized when using triangular, trapezoidal, and icosahedral shapes, in that order. The worst performance, in almost all scenarios, was predicted when using the spherical particle since it has no sharp edges.

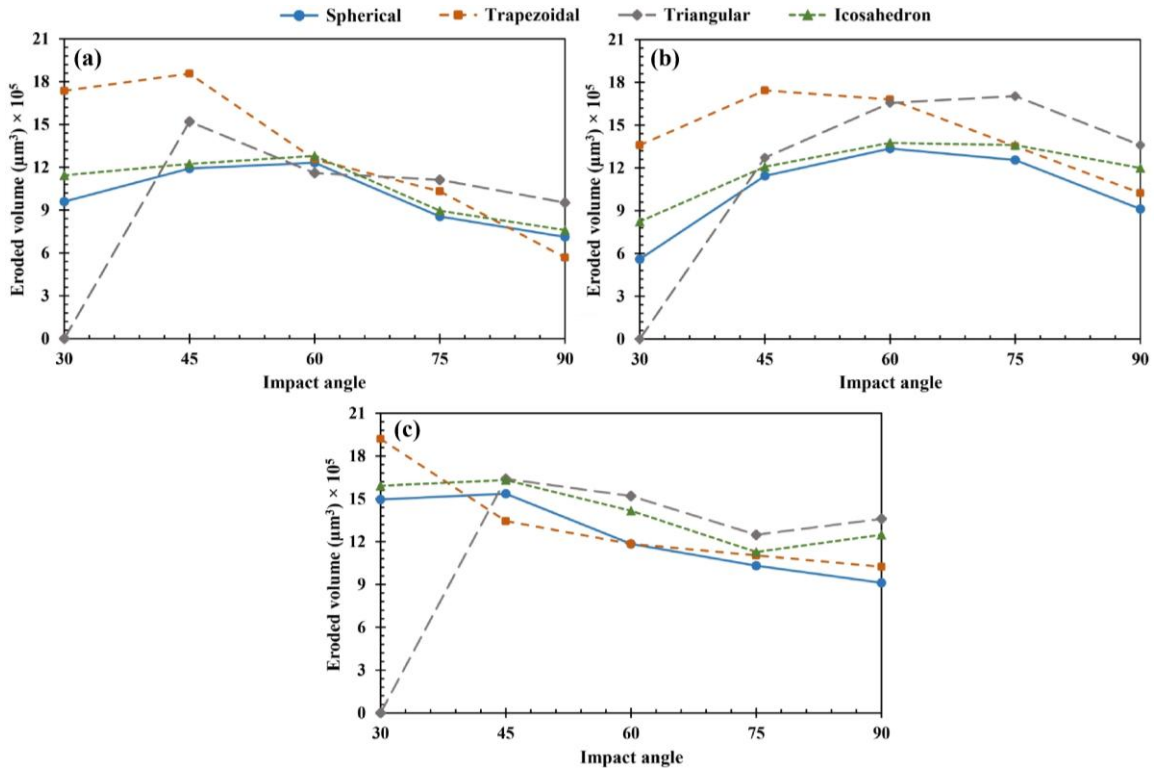

Fig. 13. The effect of using different particle shapes on the eroded volume at different impact angles while using three radial positions, (a) R_p = 0, (b) R_p = 0.42 mm, (c) R_p = -0.42 mm.

3.5 The effect of drag forces

The effect of the waterjet drag forces on the single particle mechanism was highlighted in the previous sections. This one will comprehensively investigate the presence of this effect from various aspects. For instance, Fig. 14 shows that drag forces significantly altered the particle impact position at a shallow impact angle of 30°. This drag-induced shift existed even in the normal AWJ impact over the workpiece surface but with less severity. Shifting the impact position may lead to non-uniform erosion patterns, affecting the efficiency and precision of material removal. Thence, the magnitude of the particle impact shift due to drag forces was analyzed, highlighting its dependence on impact angle and particle shape.

Fig. 15 illustrates the effect of drag forces on the particle impact shift. In this Figure, the magnitude of shift distance (Δl_d) was analyzed while varying both jet impact angle and particle shape. In general, the position at which the particle struck the workpiece differed for various particle shapes due to the presence of drag forces.

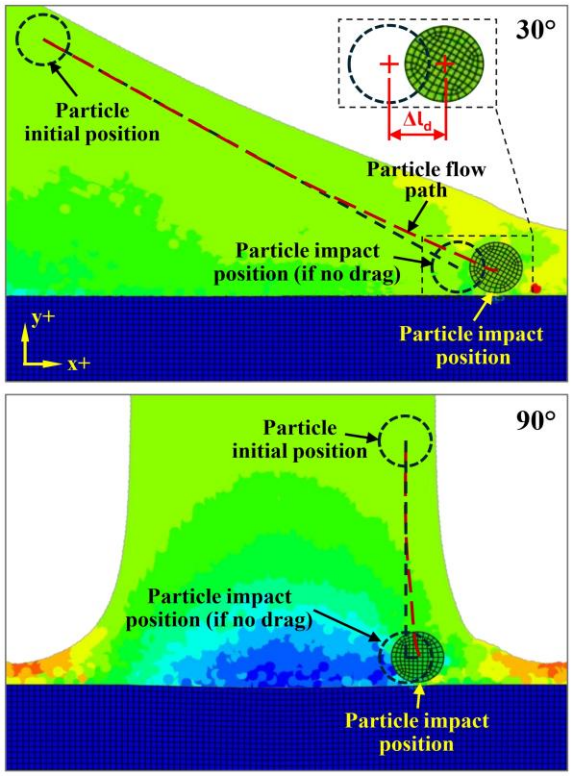

Fig. 14. Particle impact shift induced by drag forces.

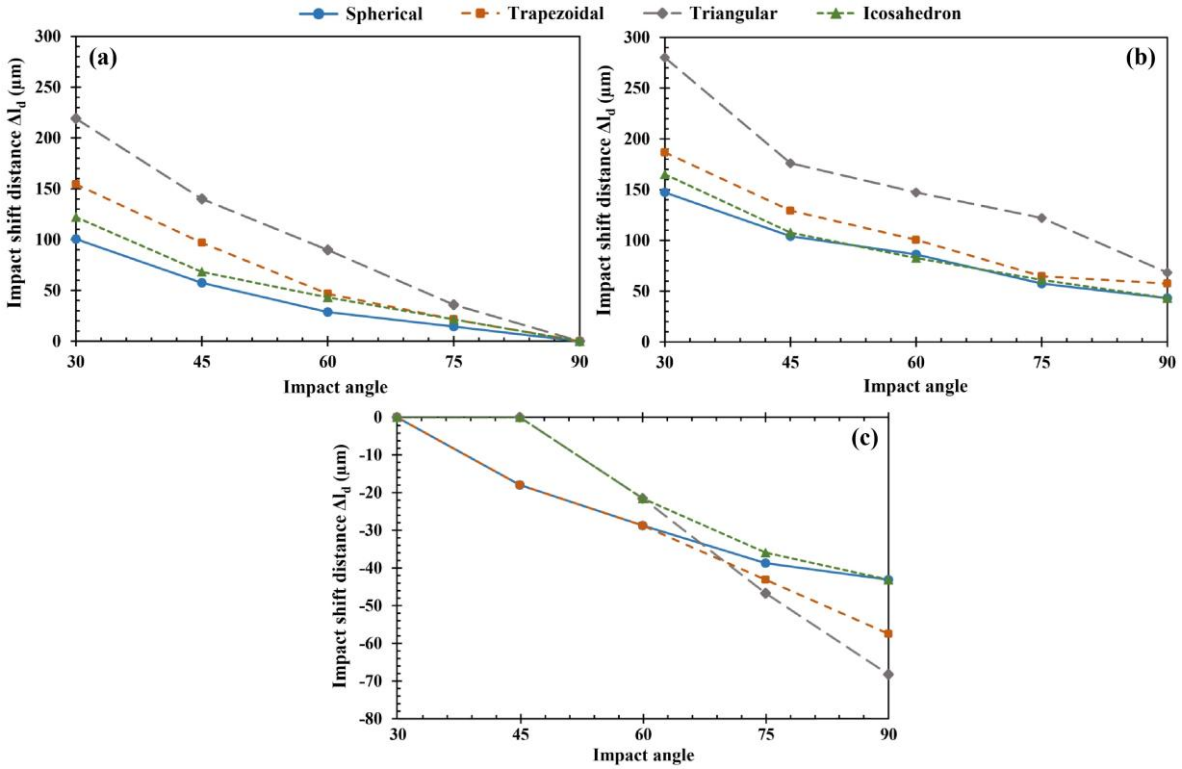

Fig. 15. Magnitude of particle impact shift at different impact angles while using three radial positions, (a) Rp = 0, (b) Rp = 0.42, (c) Rp = -0.42.

The magnitude of impact shifts was significantly dependent on particle shape with larger shifts observed when using triangular, trapezoidal, icosahedron, and sphere shapes, respectively. All particle shapes exhibited almost the same trend when varying the impact angle at radial positions of 0 mm and 0.42 mm. The impact shift was maximized at 30° and then gradually decreased

to the minimum by increasing the impact angle to 90°. On the contrary, this trend was reversed at a radial position of -0.42 mm where the maximum impact shift was achieved at 90°. It can be observed that the extent of particle shifting was reduced in the case of *R*p = -0.42 mm. This is attributed to the lower influence of drag forces, explaining the higher erosion rates generally obtained at this radial position. For all particle shapes, particle shift distance was zero at 90° and *R*p = 0 mm, implying that the effect of drag forces for normal impact was negligible at the jet center. The particle impact shift was also zero at an angle of 30° and *R*p = -0.42 mm.

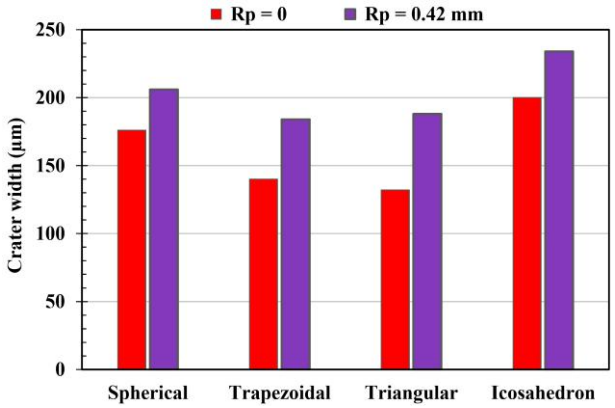

Fig. 16. Crater width at 90° and radial positions of 0 and 0.42 mm across various particle shapes.

Drag forces do not only influence the particle impact position but also can alter the crater shape. Fig. 16 compares the crater widths for radial positions of 0 and 0.42 mm at 90°. For all particle shapes, it can be demonstrated that wider craters were obtained at the jet periphery compared to the jet center. This increase in crater width was also contingent on the shape of the impacting particle. Wider craters obtained for single particle impact due to the drag forces can explain the difference in practical AWJ kerfs apart from the theoretical jet diameter.

4. CONCLUSION

An AWJM numerical model was developed to reveal the single particle impact dynamics and the corresponding erosion mechanism. Unlike the other models, the fluid-solid interaction was considered through coupling two techniques, FEM and SPH. The major conclusions of the present research study can be drawn as follows:

- Once the AWJ strikes the workpiece surface, a stagnation zone is generated and severely reducing the particle kinetic energy, which in turn hinders the erosive capability of the abrasive particle.
- An abrasive particle of a particular shape, orientation, size, and impact angle achieves different material removal rates depending on its radial position within the jet stream.
- The effect of workpiece traverse speed on erosion is insignificant even over a wide range of applicable speeds (0-125 mm/s).
- Tilting the AWJ can enhance the erosive ability of the abrasive particle as the stagnation zone effect almost disappears at shallow impact angles, but without neglecting the effect of drag forces.
- The triangular particle achieves the most effective eroding performance followed by trapezoidal, icosahedral, and spherical particles, respectively.
- The worst erosion performance, in almost all scenarios of different particle angles and radial positions, was obtained when the spherical particle was used because it has no sharp edges.
- The presence of waterjet drag forces affects the particle impact position and the resulting crater morphology.

The proposed SPH-FEM model provides valuable insights into the dynamics and material removal mechanism of single particle impact in AWJM. It serves as an important reference for analyzing and optimizing the machining process. However, the experimental confirmation of model findings presents significant challenges due to the highly dynamic, erosive, and deflective nature of the abrasive waterjet upon impact, which would cause serious damage to the sensitive measurement devices. Hence, effective experimental methods should be developed for this endeavor.

Acknowledgement

The first author is very grateful to the Egyptian Ministry of Higher Education (MoHE) for providing financial support in the form of a Ph.D. scholarship. Also, thanks to Japan International Cooperation Agency-JICA for providing all necessary facilities to accomplish this research.

REFERENCES

[1] A. W. Momber and R. Kovacevic, *Principles of abrasive water jet machining*. Springer-Verlag London, 1998. doi: 10.1007/978-1-4471-1572-4.

[2] R. Tarodiya and A. Levy, "Surface erosion due to particle-surface interactions - A review," *Powder Technology*, vol. 387, pp. 527–559, Apr. 2021, doi: 10.1016/j.powtec.2021.04.055.

[3] M. Radovanović, "Multi-objective Optimization of Process Performances when Cutting Carbon Steel with Abrasive Water Jet," *Tribology in Industry*, vol. 38, no. 4, pp. 454–462, Dec. 2016.

[4] M. Du, H. Wang, H. Dong, Y. Guo, and Y. Ke, "Numerical research on multi-particle movements and nozzle wear involved in abrasive waterjet machining," *The International Journal of Advanced Manufacturing Technology*, vol. 117, no. 9, pp. 2845–2858, Aug. 2021, doi: 10.1007/s00170-021-07876-9.

[5] B. Jelena, N. Bogdan, and M. Vlatko, "Focusing tube wear and quality of the machined surface of the abrasive water jet machining," *Tribology in Industry*, vol. 30, no. 3–4, pp. 55–58, Sep-Dec. 2008.

[6] A. I. Hassan and J. Kosmol, "Dynamic elastic–plastic analysis of 3D deformation in abrasive waterjet machining," *Journal of Materials Processing Technology*, vol. 113, no. 1-3, pp. 337–341, Jun. 2001, doi: 10.1016/S0924-0136(01)00687-2.

[7] M. Junkar, B. Jurisevic, M. Fajdiga, and M. Grah, "Finite element analysis of single-particle impact in abrasive water jet machining," *International Journal of Impact Engineering*, vol. 32, no. 7, pp. 1095–1112, Dec. 2004, doi: 10.1016/j.ijimpeng.2004.09.006.

[8] B. Yıldırım and S. Müftü, "Simulation and analysis of the impact of micron-scale particles onto a rough surface," *International Journal of Solids and Structures*, vol. 49, no. 11-12, pp. 1375–1386, Mar. 2012, doi: 10.1016/j.ijsolstr.2012.02.018.

[9] X. Dong, Z. Li, L. Feng, Z. Sun, and C. Fan, "Modeling, simulation, and analysis of the impact(s) of single angular-type particles on ductile surfaces using smoothed particle hydrodynamics," *Powder Technology*, vol. 318, pp. 363–382, Jun. 2017, doi: 10.1016/j.powtec.2017.06.011.

[10] Y. Abdelhameed, I. Maher, J. Yan, H. El-Hofy, and M. A. Hassan, "Finite element analysis of material removal in AWJM using different material models and spatial distributions for garnet abrasives," *International Journal of Machining and Machinability of Materials*, vol. 1, no. 1, Nov. 2024, doi: 10.1504/IJMMM.2025.10068145.

[11] X. Dong, Z. Li, C. Jiang, and Y. Liu, "Smoothed particle hydrodynamics (SPH) simulation of impinging jet flows containing abrasive rigid bodies," *Computational Particle Mechanics*, vol. 6, no. 3, pp. 479–501, Feb. 2019, doi: 10.1007/s40571-019-00227-2.

[12] J. Nyaboro, M. Ahmed, H. El-Hofy, and M. El-Hofy, "Experimental and numerical investigation of the abrasive waterjet machining of aluminum-7075-t6 for aerospace applications," *Advances in Manufacturing*, vol. 9, no. 2, pp. 286–303, Jan. 2021, doi: 10.1007/s40436-020-00338-7.

[13] M. Du, K. Zhang, Y. Liu, L. Feng, and C. Fan, "Experimental and simulation study on the influence factors of abrasive water jet machining ductile materials," *Energy Reports*, vol. 8, pp. 11840–11857, Sep. 2022, doi: 10.1016/j.egyr.2022.09.035.

[14] B. Vasudevan, Y. Natarajan, R. Pavan Kumar, K. Umesh Chandra, and D. Sikder, "Simulation of AWJ drilling process using the fea coupled sph models: a preliminary study," *Materials Today Proceedings*, vol. 62, pp. 6022–6028, Jan. 2022, doi: 10.1016/j.matpr.2022.04.990.

[15] M. B. Liu and G. R. Liu, "Smoothed Particle Hydrodynamics (SPH): an Overview and Recent Developments," *Archives of computational methods in engineering*, vol. 17, no. 1, pp. 25–76, Feb. 2010, doi: 10.1007/s11831-010-9040-7.

[16] M. Mu, L. Feng, Q. Zhang, W. Zang, and H. Wang, "Study on abrasive particle impact modeling and cutting mechanism," *Energy Science & Engineering*, vol. 10, no. 1, pp. 96–119, Dec. 2021, doi: 10.1002/ese3.1012.

[17] G. R. Johnson and W. H. Cook, "A constitutive model and data for metals subjected to large strains, high strain rates and high temperatures," *in 7th International Symposium on Ballistics*, pp. 541–547, Apr. 1983.

[18] G. R. Johnson and W. H. Cook, "Fracture characteristics of three metals subjected to various strains, strain rates, temperatures and pressures," *Engineering Fracture Mechanics*, vol. 21, no. 1, pp. 31–48, Jan. 1985, doi: 10.1016/0013-7944(85)90052-9.

[19] A. Sharma, R. Mishra, S. Jain, S. S. Padhee, and P. K. Agnihotri, "Deformation behavior of single and multi-layered materials under impact loading," *Thin-Walled Structures*, vol. 126, pp. 193–204, Aug. 2018, doi: 10.1016/j.tws.2017.08.021.

[20] D.-N. Zhang, Q.-Q. Shangguan, C.-J. Xie, and F. Liu, "A Modified Johnson–Cook Model of Dynamic Tensile Behaviors for 7075-T6 Aluminum Alloy," *Journal of Alloys and Compounds*, vol. 619, pp. 186–194, 2015, doi: 10.1016/j.jallcom.2014.09.002.

[21] Y. Abdelhameed, A. I. Hassan, and S. Kaytbay, "A user-friendly finite element model for radial mode abrasive waterjet turning," *Proceedings of the Institution of Mechanical Engineers, Part B: Journal of Engineering Manufacture*, vol. 235, no. 12, pp. 1904–1916, May 2021, doi: 10.1177/09544054211017305.

[22] H. Hibbitt, B. Karlsson, and P. Sorensen, *Abaqus analysis user's manual*. Vélizy-Villacoublay: Dassault Systemes, 2011.

[23] M. Demiral, F. Abbassi, T. Saracyakupoglu, and M. Habibi, "Damage analysis of a CFRP cross-ply laminate subjected to abrasive water jet cutting," *Alexandria Engineering Journal*, vol. 61, no. 10, pp. 7669–7684, Jan. 2022, doi: 10.1016/j.aej.2022.01.018.

[24] B. D. Nandre and G. R. Desale, "Role of particle shape on slurry erosion wear of AA6063," *Tribology in Industry*, vol. 45, no. 3, pp. 522–531, Sep. 2023, doi: 10.24874/ti.1503.06.23.08.

[25] L. M. Hlaváč et al., "Comminution of material particles by water jets — Influence of the inner shape of the mixing chamber," *International Journal of Mineral Processing*, vol. 95, no. 1-4, pp. 25–29, Mar. 2010, doi: 10.1016/j.minpro.2010.03.003.

[26] L. Gembalová, L. M. Hlaváč, S. Spadło, V. Geryk, and L. Oros, "Notes on the abrasive water jet (awj) machining," *Materials*, vol. 14, no. 22, p. 7032, Nov. 2021, doi: 10.3390/ma14227032.

[27] L. Feng, G. R. Liu, Z. Li, X. Dong, and M. Du, "Study on the effects of abrasive particle shape on the cutting performance of ti-6al-4v materials based on the sph method," *The International Journal of Advanced Manufacturing Technology*, vol. 101, no. 9-12, pp. 3167–3182, Dec. 2019, doi: 10.1007/s00170-018-3119-y.

[28] M. Du, H. Wang, H. Dong, Y. Guo, and Y. Ke, "Numerical research on kerf characteristics of abrasive waterjet machining based on the sph-dem-fem approach," *The International Journal of Advanced Manufacturing Technology*, vol. 111, no. 11, pp. 3519–3533, Nov. 2020, doi: 10.1007/s00170-020-06340-4.

[29] S. Rammohan, S. T, Kumaran, M. Uthayakumar, and A. Velayutham, "Numerical modeling of kerf generation in abrasive waterjet machining of military grade armor steel," *Human Factors and Mechanical Engineering for Defense and Safety*, vol. 7, no. 1, p. 1, 2023, doi: 10.1007/s41314-023-00056-5.